ACS OMEGA

http://pubs.acs.org/journal/acsodf

Article

Electrocatalysis of Endosulfan Based on Fe_3O_4: An Experimental and Computational Approach

Gloria Uwaya, Njabulo Joyfull Gumede, and Krishna Bisetty*

Cite This: *ACS Omega* 2021, 6, 30515−30525

Read Online

ACCESS | Metrics & More | Article Recommendations

ABSTRACT: The present work reports the electrocatalytic oxidation of the organochlorine pesticide endosulfan (EDS) using iron oxide (Fe_3O_4) nanoparticles synthesized from *Callistemon viminalis* leaf extracts. As a sensor for EDS, Fe_3O_4 was combined with functionalized multiwalled carbon nanotubes (f-MWCNTs) on a glassy carbon electrode (GCE). Cyclic voltammetry, electrochemical impedance spectroscopy, and the differential pulse voltammetry experiment were conducted to investigate the electrochemistry of EDS on the GCE/f-MWCNT/Fe_3O_4 sensor. Based on optimized experimental conditions, the reports of analytical parameters show a limit of detection of 3.3 μM and an effective sensitivity of 0.06464 μA/μM over a range of concentrations from 0.1 to 20 μM. With the proposed method, we were able to demonstrate recoveries between 94 and 110% for EDS determinations in vegetables. Further, a series of computational modeling studies were carried out to better understand the EDS surface adsorption phenomenon on the GCE/f-MWCNT/Fe_3O_4 sensor. The highest occupied molecular orbital−lowest unoccupied molecular orbital (HOMO−LUMO) energy gap (−5.18 eV) computed by density functional theory (DFT) supports the layer-by-layer electrode modification strategy's charge transfer and stability. Finally, transition state modeling was able to predict and confirm the mechanism of endosulfan oxidation.

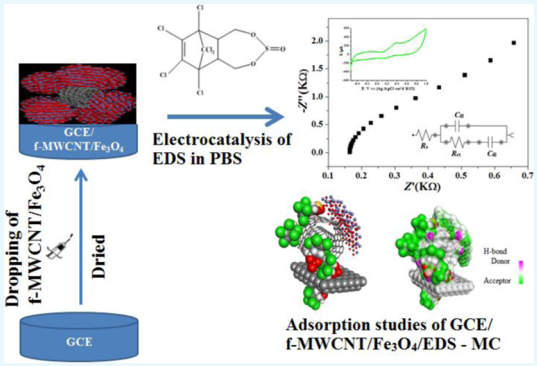

1. INTRODUCTION

The organochlorine insecticide endosulfan (EDS) (Figure 1a) is used as part of a crop production strategy to control insects, termites, and any other pests that may reduce yields.[1−4] Figure 1b,c shows that EDS is commercially available in mixtures of isomers and is considered an organic pollutant because it bioaccumulates. EDS is probably carcinogenic, based on EPA guidelines,[5] and acutely toxic according to the US Environmental Protection Agency (USEPA). Accordingly, the Stockholm Convention 2011 has prohibited the use of EDS in all countries but the practice is still legal in some countries.[6,7]

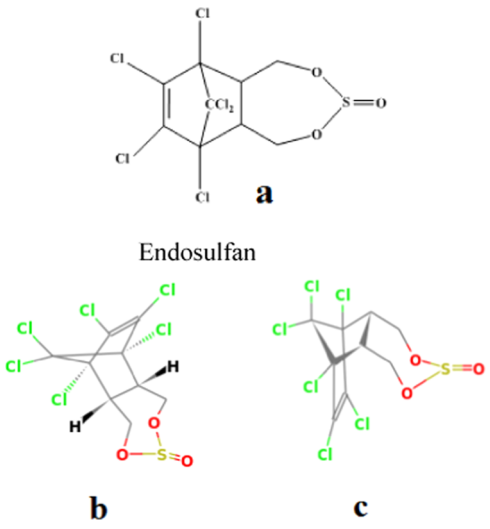

Figure 1. Chemical structures of (a) endosulfan and (b, c) its stereoisomer.

Using EDS excessively and misusing it negatively impacts our health, environment, and ecosystem. This causes endocrine disruption. In addition to birth defects, respiratory failure, biochemical instability, kidney, hepatic, and cardiac toxicities with symptoms of nausea, vomiting, tremors, and hypotension. EDS can also cause birth defects and respiratory failure.[1,2,8,9] Moreover, the discharge of EDS into fresh and groundwater as spray drifts and runoffs and its presence in food pose concerns since it can pose risks to humans and other organisms if inhaled, absorbed, and ingested from diverse sources of food chains.[1,2] Monitoring endosulfan residues in water, soil, and

Received: July 26, 2021
Accepted: October 8, 2021
Published: November 3, 2021

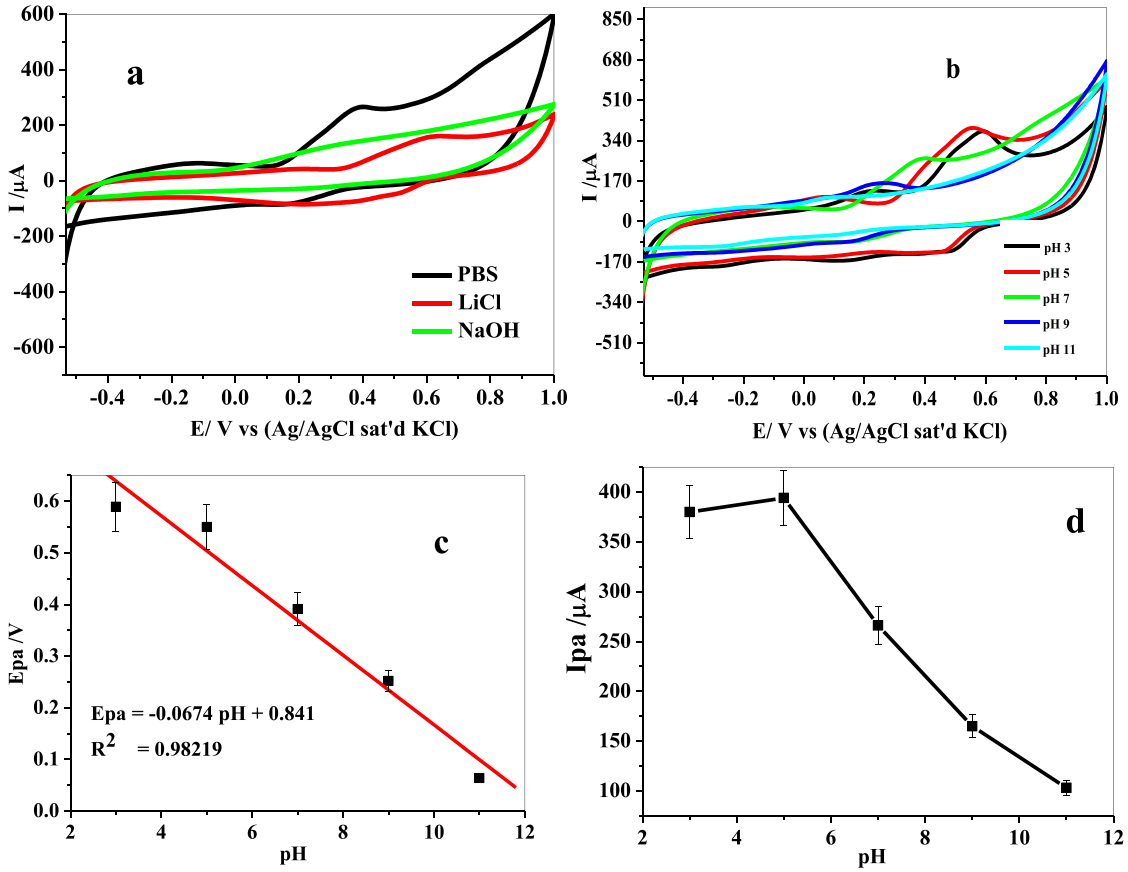

Figure 2. Effect of (a) the supporting electrolyte and (b) pH for 36 μM EDS in 0.1 M PBS at a scan rate of 25 mV s^{-1}. Linear plots of (c) E_{pa} vs pH and (d) I_{pa} against pH.

food is crucial for maintaining public health and the health of ecosystems. Various analytical techniques have been used for EDS detection, including chromatography,[10−14] immunosensors,[3] and electrochemical sensors.[1,2,8,15,16] Compared to chromatographic methods, immunosensors are uneconomical with poor sensitivity and specificity as a result of the cost and denaturation of enzymes and require expertise, large samples, and a long time to perform.[1] Electrochemical sensors, on the other hand, offer a method that is accessible, fast, easy to use, low cost, sensitive, and reproducible to overcome these limitations. The literature search revealed that there are many articles on electrochemical detection but a few on EDS. A variety of nanostructured materials are used to modify electrodes, including carbon nanotubes (multiwalled carbon nanotubes (MWCNTs) and single-walled carbon nanotubes), metal oxides, and polymers. Materials such as these are used as electrode modifiers due to their biocompatibility, strong adsorption ability, nontoxicity, catalytic activity, and improved electron transfer kinetics.[15,17−20]

As a result of their good electrical conductivity and ability to adhere to the electrode surface, multiwalled carbon nanotubes (MWCNTs) are widely used in electrochemical sensors.[21,22] Furthermore, acid functionalization of MWCNTs can lead to improved ion exchange and activation.[23−25] Iron(III) oxide (Fe_3O_4) nanoparticles (NPs) are widely used in sensing due to their supermagnetism, ferromagnetism, biocompatibility, ease of preparation at low cost, nontoxicity, electrical conductivity, and large surface area.[26] As a result, the combination of MWCNTs and Fe_3O_4 nanoparticles in sensors was shown to enhance the electrode performance greatly. In the detection of dopamine, choline, nitrite, and sunset yellow, the nanocomposite of Fe_3O_4/MWCNTs has been used.[27−29] Several studies have used Fe_3O_4/MWCNT/laser graphene, and Fe_3O_4/MWCNT/polyacrylonitrile composites for cadmium, lead, and 3-methoxyphenol detection.[30,31]

The purpose of this study was to design a sensor with a fast response time for monitoring EDS in foods based on the synthesis of a nanocomposite of functionalized MWCNT (f-MWCNT) and Fe_3O_4 nanoparticles using *Callistemon viminalis* leaf extract. For the first time, we have combined computational and experimental approaches and used density functional theory (DFT) calculations, Monte Carlo (MC) adsorption studies, and transition state modeling to verify the electrochemical fabrication of the sensor.

2. RESULTS AND DISCUSSION

2.1. Experimental Section. *2.1.1. Effect of the Supporting Electrolyte.* To demonstrate that the peak current of an analyte depends strongly on the supporting electrolyte, the current response for EDS was examined in different supporting electrolyte solutions such as 0.1, 0.075, and 0.01 M phosphate buffer saline (PBS), lithium chloride, and sodium hydroxide, respectively, using cyclic voltammetry (CV) at a scan rate of 25 mV s^{-1}. A strong oxidation peak current for EDS was observed in PBS buffer (Figure 2a), and thus, PBS was chosen throughout the experiment.

2.1.2. Effect of pH. The voltammetric response of the electrooxidation of EDS at the glassy carbon electrode (GCE)/MWCNT/Fe_3O_4 nanocomposite was studied in PBS buffer at

https://doi.org/10.1021/acsomega.1c03995
ACS Omega 2021, 6, 30515−30525

Scheme 1. Schematic Illustration of a Stepwise Electrode Modification for the Electrocatalysis of EDS

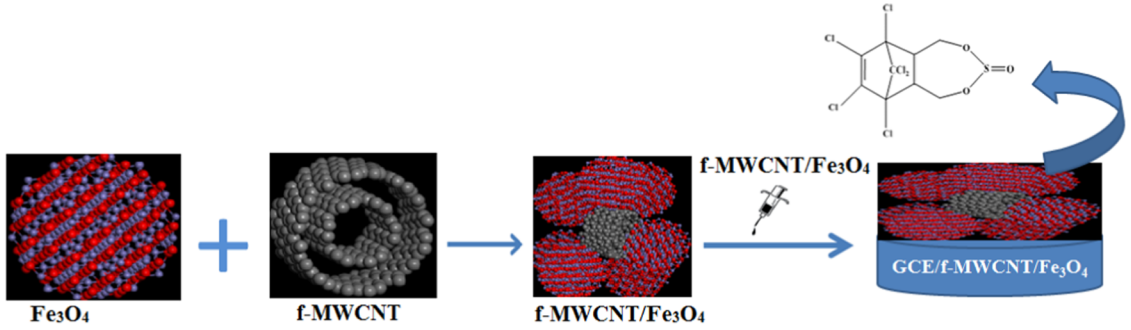

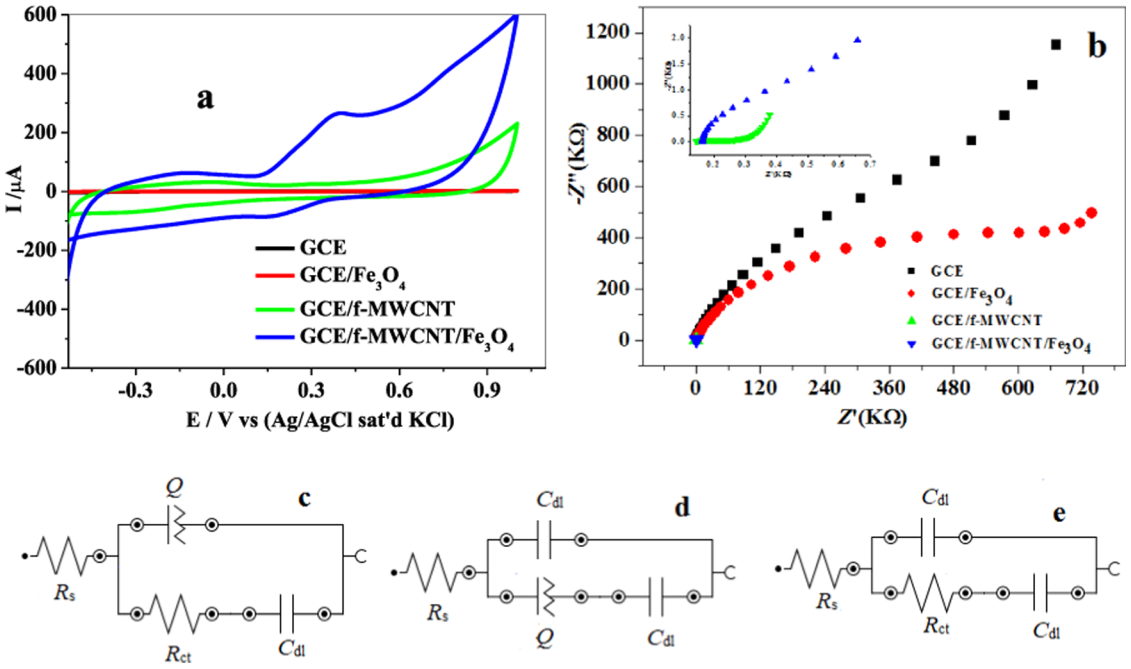

Figure 3. (a–e) Comparative cyclic voltammograms for bare GCE and modified electrodes at 25 mV s^{-1} and (b) Nyquist plots for the electrodes in 0.1 M PBS at pH 7 containing 36 μM EDS. (c–e) Circuits used in the fitting of EIS data for GCE and GCE/Fe_3O_4, GCE/f-MWCNT, and GCE/f-MWCNT/Fe_3O_4, respectively.

Table 1. Summary of Equivalent Circuit Parameters from Impedance Spectra Fitting

electrodes	R_s (KΩ)	R_{ct} (KΩ)	C_{dl} (μF)	χ^2
GCE	0.217 (2.94)	1830 (10.6)	0.972 (18.0)	0.539
GCE/Fe_3O_4	0.264 (3.22)	989 (5.13)	4.03 (23.7)	0.581
GCE/f-MWCNT	0.144 (2.73)		3420 (7.67)	0.559
GCE/f-MWCNT/Fe_3O_4	0.165 (1.43)	4.32 (21.2)	383 (31.2)	0.544

pH ranging from 3 to 11 at a sweep rate of 25 mV s^{-1} and a potential window ranging from −0.53 to −1 V (Figure 2a).

The optimum current response for the analyte was found at pH 5 (Figure 2d); however, the expected potential for the analyte was found at pH 7, which was subsequently used in this study. As shown in Figure 2c, the E_{pa} vs pH plot has a slope of −0.0674 and is in good agreement with the theoretical value reported (−0.059 V pH^{-1}),[32] proving a two-electron, two-proton transfer process in EDS.

2.1.3. Electrochemical Properties of Endosulfan. The electrochemical behavior of EDS on bare and modified electrodes was examined using cyclic voltammetry (CV) and electrochemical impedance spectroscopy (EIS) in 36 μM EDS solution in PBS buffer at pH 7. Scheme 1 summarizes the electrode (GCE/f-MWCNT/Fe_3O_4) modification process.

2.1.4. Electrocatalytic Oxidation of Endosulfan. Figure 3a shows the electrochemical behavior of endosulfan on the modified electrodes (GCE/Fe_3O_4, GCE/f-MWCNT, and GCE/f-MWCNT/Fe_3O_4) investigated using CV at a scan rate of 25 mV s^{-1}. The CV results demonstrated that EDS displayed a capacitive current for GCE/f-MWCNT and an irreversible oxidation behavior at 0.39 V for the GCE/f-MWCNT/Fe_3O_4 electrode. This result is similar to the potential (0.4 V) at which endosulfan was reported in the literature.[1] Furthermore, our comparative results suggest that the oxidation at the GCE/f-MWCNT/Fe_3O_4 electrode could

https://doi.org/10.1021/acsomega.1c03995
ACS Omega 2021, 6, 30515−30525

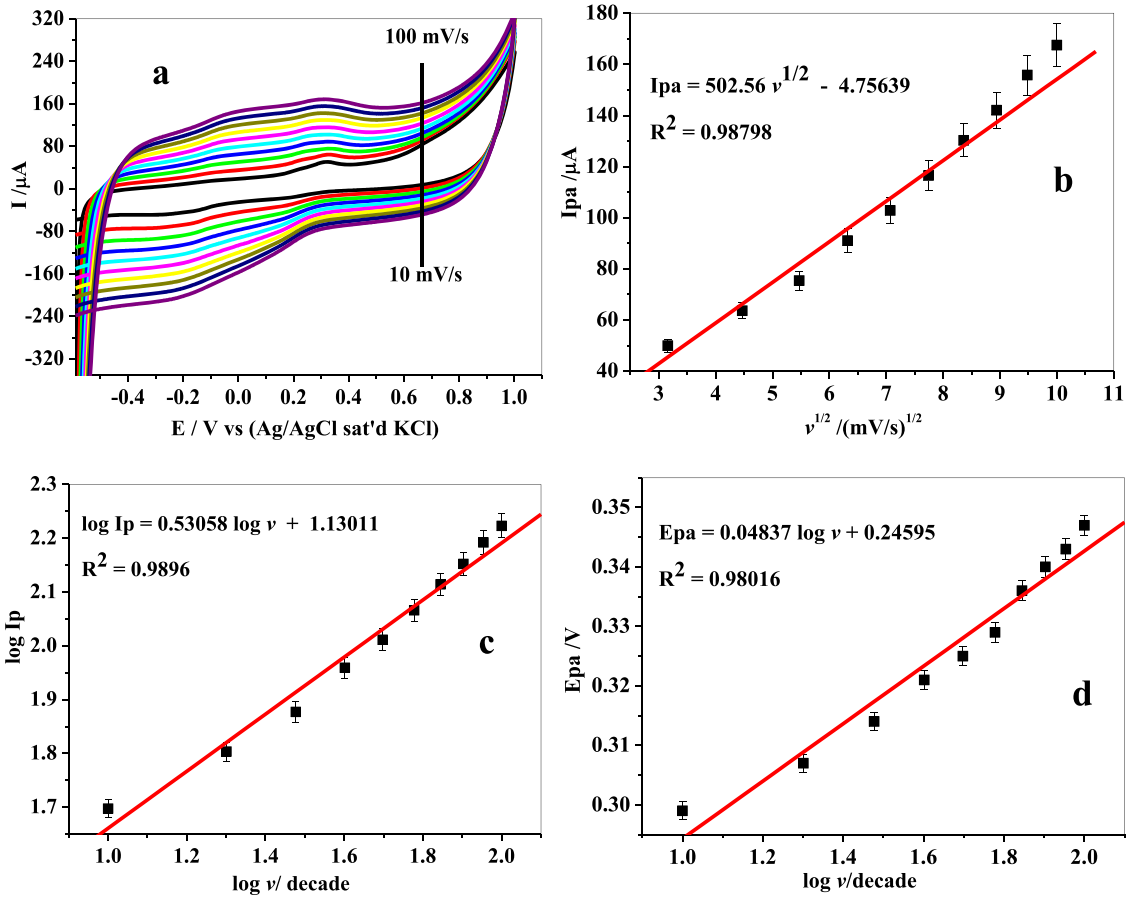

Figure 4. (a) Cyclic voltammogram of the GCE/f-MWCNT/Fe_3O_4 electrode at different scan rates in PBS buffer at pH 7 containing 36 μM EDS. (b) Linear relation between (I_{pa}) and $v^{1/2}$. (c) Linear relationship between log I_{pa} and log v. (d) Linear relation between (E_{pa}) and log v.

be attributed to the electronic conductivity and reactivity of Fe_3O_4, enhanced by the presence of f-MWCNT.

The mechanism of the electron transport and the characteristics of the electrode interface during the electrocatalytic oxidation of 36 μM EDS at 0.4 V and frequencies between 100 kHz and 0.1 Hz were monitored using EIS. The Nyquist plots (impedance spectra) for the electrodes are shown in Figure 3b, while the equivalent circuits used in the spectra modeling after repeated fittings are shown in Figure 3c−e. The EIS spectra of GCE/f-MWCNT and GCE/f-MWCNT are shown (inset of Figure 3b) since they are less vivid as a result of their real (Z') values being <1 kΩ. Table 1 presents the chi-squared (χ^2) values (estimated errors) of all fitted spectra conclusively proving successful fitting. It shows the circuit parameters obtained from the fit of impedance spectra. The parameters R_s, R_{ct}, Q, and C_{dl} indicate solution resistance, saturated charge transfer, constant phase element, and double-layer capacitance, respectively. GCE/f-MWCNTs exhibit a greater C_{dl} value, suggesting greater charge accumulation and superior conductivity.[21] The capacitive current measured in CV could be the consequence of this. As shown in Figure 3a, the R_{ct} value of the f-MWCNT/Fe_3O_4 electrode is lower than the R_{ct} values for other electrode types, indicating a fast electron transport.[21,33]

2.1.5. Influence of Varying Scan Rates at Constant EDS. To examine the type of electrode reaction occurring at the electrode surface, the effect of scan rate variation on the current response of EDS was studied. The CV response of the nanocomposite-modified electrode (GCE/f-MWCNT/Fe_3O_4) at different scan rates (10−100 mV s^{-1}) recorded in 0.1 M PBS (pH 7) containing 36 μM EDS is shown in Figure 4a. A linear oxidation peak current response was observed when the oxidation peak potentials shifted positively, suggesting a decrease in the electron transfer rate.[32] The oxidation peak current (I_{pa}) increases linearly as the square root of scan rate ($v^{1/2}$) is increased. The linear regression equation with R^2 0.98798 represents the diffusion-controlled electrochemical process shown in Figure 4b. In addition, the plot of a logarithm of the peak current against a logarithm of scan rate is linear (Figure 4c) with a slope of 0.53058, demonstrating that the process exhibits a diffusion-controlled process.[34]

Figure 4d represents the plot of E_{pa} vs logarithm of scan rate with a slope of 0.04837. Based on the slope value and using eq 1, the Tafel slope (Figure 4b) was found to be 0.097 V dec^{-1}, which is less than the theoretical value (0.118 V dec^{-1}), indicating the absence of adsorption on the electrode surface.

$$E_p = \frac{b}{2}\log v + \text{constant} \quad (1)$$

The charge transfer coefficient (α), number of electrons (n) involved in the rate-determining step, and the charge transfer rate constant (ks) were evaluated. The value of the charge transfer coefficient (α) was calculated to be 0.39 using eq 2.[35]

$$\propto = \frac{47.7}{E_p - E_{p/2}}\text{mV} \quad (2)$$

where E_p is the value of the oxidation peak potential and $E_{p/2}$ is the potential at which the current is at half peak value. The

https://doi.org/10.1021/acsomega.1c03995
ACS Omega 2021, 6, 30515−30525

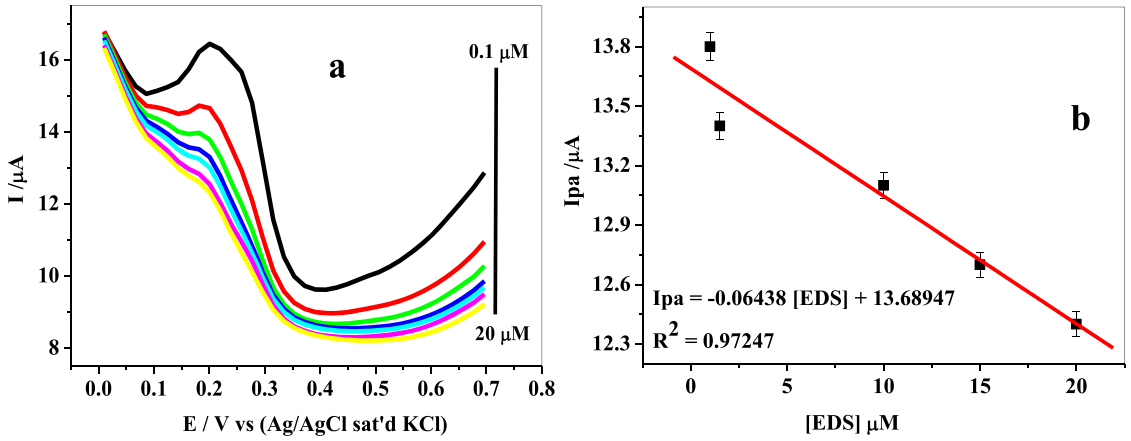

Figure 5. (a) Successive differential pulse voltammograms on GCE/f-MWCNT/Fe_3O_4 for (0.1−20 μM) [EDS]. (b) Linear relationship between I_{pa} and [EDS].

number of electrons transferred in the electrooxidation of EDS was estimated to be 2.027 by applying eq 3.

$$b = \frac{2.303RT}{(1 - \alpha)nF} \tag{3}$$

where b, R, T, and F are the slope of Figure 4d, gas constant (8.314 J $Kmol^{-1}$), temperature (298 K), and Faraday constant (96500 C mol^{-1}), respectively. The obtained n is approximately 2, which supports the coupled two-electron and two-proton process for EDS suggested by the slope value of E_{pa} vs pH (Figure 1). The value of ks was estimated to be 6.09×10^{-4} s^{-1} by applying eq 4.

$$\log ks = \alpha \log(1 - \alpha) + (1 - \alpha)\log \alpha - \log \frac{RT}{nFv} - \alpha (1 - \alpha)\frac{nFEp}{2.3RT} \tag{4}$$

In addition, the surface concentration (Γ) of the electroactive species (EDS) on the GCE/f-MWCNT/Fe_3O_4 electrode surface was found to be 4.94×10^{-3} mol cm^{-2} from the slope value of the linear equation 5 derived from the graph of peak current versus scan rate (graph not shown) using eq 6.

$$I_p = 1313.9\, v + 37.2;\ R^2 = 0.99978 \tag{5}$$

$$I_p = \frac{n^2F^2Av}{4RT} \tag{6}$$

Furthermore, the value of diffusion coefficient (7.76×10^{-4} cm^2 s^{-1}) for EDS oxidation was calculated based on the slope value of Figure 4b by applying the Randles−Sevcik equation 7 for an irreversible electrochemical process.

$$I_p = (2.999\times 10^5)n[1 - \alpha]n]^{1/2}ACD^{1/2}v^{1/2} \tag{7}$$

where A is the electrode area (cm^2), C is the bulk concentration of EDS in mol cm^{-3}, D is the diffusion coefficient in cm^2 s^{-1}, and v is the scan rate (V s^{-1}).

2.1.6. Differential Pulse Voltammetric (DPV) Detection of EDS. The linear concentration range, detection limit, and sensitivity of EDS at GCE/f-MWCNT/Fe_3O_4 were determined using DPV. Figure 5 shows a decrease in oxidation peak currents with increasing EDS concentrations ranging from 0.1 to 20 μM with a sensitivity of 0.064 μA/μM, similar to those reported in the literature.[8] The limit of detection (LoD) and quantification (LoQ) for EDS were 3.3 and 11 μM based on LoD = $\frac{3.3S}{m}$ and LoQ = $\frac{10S}{m}$, respectively, where s is the standard deviation of the intercept of the y-coordinates from the line of the best fit of the calibration plot (Figure 5b) and m is the slope of the same line. The LoD compared well with that of the molecularly imprinted polymer (MIP)[2] and antimony polyaniline single-walled carbon nanotube nanocomposite[8] (Sb_2ONP-PANI-SWCNT)-modified electrodes (20, 6.8 μM, respectively).[2,8]

However, it was higher than the LoD (0.02 μM) of an immunosensor based on a 4-aminophenyl/single-walled carbon nanotube/2-(2-(2-(4-aminophenoxy)ethoxy)ethoxy) ethanol/ferrocenedimethylene-modified glassy carbon electrode (GCE/Ph-NH_2/SWCNT/PEG/FDMA)[3] presented in Table 2, involving a complex sensor with multiple coupling steps.

Table 2. Comparison of the Designed Sensor with Other Reported EDS Sensors

sensors	linearity (μM)	LoD (μM)	ref
MIP	20−120	20.0	2
AONP-PANI-SWCNT	32.3−77.6	6.8	8
Ph-NH_2/SWCNT/PEG/FDMA	0.025−49.2	0.02	3
GCE/f-MWCNT/Fe_3O_4	0.1−20	3.3	this work

2.1.7. Repeatability, Reproducibility, and Stability of the Electrode. The repeatability of the designed sensor (GCE/f-MWCNT/Fe_3O4) was examined using CV for 15 repetitive scans in 36 μM EDS. A drop of about 13.9% in the peak current was observed, indicating acceptable stability. Reproducibility studies with the same EDS concentration using two different electrodes for three repetitive measurements gave RSDs of 3.45 and 3.74%, respectively, indicating good reproducibility. The electrode storage stability was also studied using DPV in the same aforementioned EDS concentration. GCE/f-MWCNT/Fe_3O_4 was stored in the refrigerator at 4 °C when not in use. The current response was investigated after 5 and 10 days resulting in 78 and 68% responses, respectively. The electrode was stored in the refrigerator when not in use. An interference study was conducted using chronoamperometry (CA) to investigate the selectivity of the electrode in the presence of the possible interfering species. Figure 6 presents

https://doi.org/10.1021/acsomega.1c03995
ACS Omega 2021, 6, 30515−30525

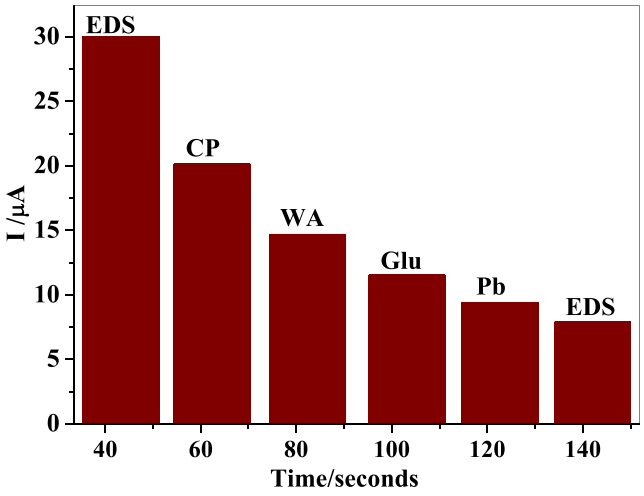

Figure 6. Histogram from current−time curve for the selectivity studies of the GCE/f-MWCNT/Fe_3O_4 electrode.

the current−time curve in histogram recorded from CA. EDS signal was determined prior to and after adding chlorpyrifos (CP), warfarin (WA), glucose (Glu), and lead (Pb), each at the same concentration (100 μM), into 0.1 M PBS solution at pH 7. From the current−time curve represented with a histogram, the current response of EDS could also be seen after the injection of possible interfering species, suggesting selectivity of the electrode.

2.1.8. Analytical Performance of the Designed Sensor for EDS Determination in Vegetable (Tomatoes). The analytical applicability of the developed sensor for the determination of EDS in tomato samples was investigated using a standard addition of the prepared solution of endosulfan. The effect of matrix and concentration was evaluated by spiking the real tomato samples with a known concentration of endosulfan. The experimental results (Table 3) displayed satisfactory recoveries with reasonable relative standard deviation values, demonstrating the applicability and reproducibility of the developed sensor for EDS determination.

Table 3. Practical Application of GCE/f-MWCNT/Fe_3O_4

samples	added (μM)	found (μM)	recovery (%)	RSD (N = 3)
tomatoes	1.71	1.71	100	1.80
	2.51	2.78	110	0.41
	4.00	3.76	94	0.34

2.2. Computational Results. *2.2.1. DFT Calculations.* Figure 7a,b presents the calculated IR spectra of EDS reactants and products computed at the B3LYP/6-31+G* level based on the model structure of EDS optimized at the same level of theory. The stretching vibrational frequencies for Figure 7a were found at 640 cm^{-1}, which were assigned to O−S−O of the sulfite group, whereas the calculated values at 1025 and 1241 cm^{-1} are the bands typical of the C−O and S═O stretchings, respectively. On the other hand, the calculated vibrational spectrum of the EDS products in Figure 7b is dominated by a band at 667 cm^{-1}, which corresponds to the out-of-plane bending of the C−H bonds; other important features are the bands typical of the S−O stretching at 687 cm^{-1} and the O−H stretching vibration at 761 cm^{-1}. Finally, the peaks related to the in-plane bending of the O−H and S−O bonds are located around 1000 cm^{-1}.

To describe the reactivity of EDS, the band gap energy was calculated as the difference between the highest occupied molecular orbit (HOMO) and the lowest unoccupied molecular orbit (LUMO) (Figure 8). The energy gap between HOMO−LUMO indicates the molecular chemical stability. The red color indicates a negative charge and the green color indicates a positive charge. We obtained a HOMO−LUMO gap of −5.81 eV for an isolated EDS molecule, indicating a charge transfer within the molecule.

2.2.2. Transition State Modeling. To model the mechanism for the transformation of EDS to form the product (1,4,5,6,7,7-hexachloro-3-methylidenebicyclo[2.2.1]hept-5-*en*-2-yl) methyl hydrogen sulfite (Scheme 2), the Auto TS module was implemented using Jaguar.[36] A DFT simulation at a B3LYP level of theory and the 61-31G+* basis set was performed using water as a solvent. The Auto TS simulation predicted the mechanism for this transformation, notably by the presence of six transition states observed in Figure 9, with the reactant and product set at reaction energies of 0.00 and 104.84 kcal mol^{-1}, respectively. This indeed indicates that the reaction is thermodynamically favorable.

Figure 9 shows the first transition state (TS1) with the reaction energy of 197.05 kcal mol^{-1}, caused by a series of bond dissociation at C(19) resulting in the cyclopropyl ring formation with C(5), C(6), and C(7); the bonding of S(2) with O(1), O(3), and O(18) atoms and the heterolytic bond dissociation of the Cl group bonded to C(5). This isomer is unstable as evidenced by the high reaction energy, a HOMO−LUMO gap of −0.0914 eV, and a solvation energy of −22.67 kcal mol^{-1} (Table 4).

The second transition state (TS2), with a slightly lower energy of 183.07 kcal mol^{-1}, is attributed to the breaking of the C(5)−Cl(18) and C(6)−H(23) bonds; a π bond between O(18)−C(19) S(2). The formation of σ bonding is observed in O(1)−C(19) and with S(2)−O(18). Furthermore, a

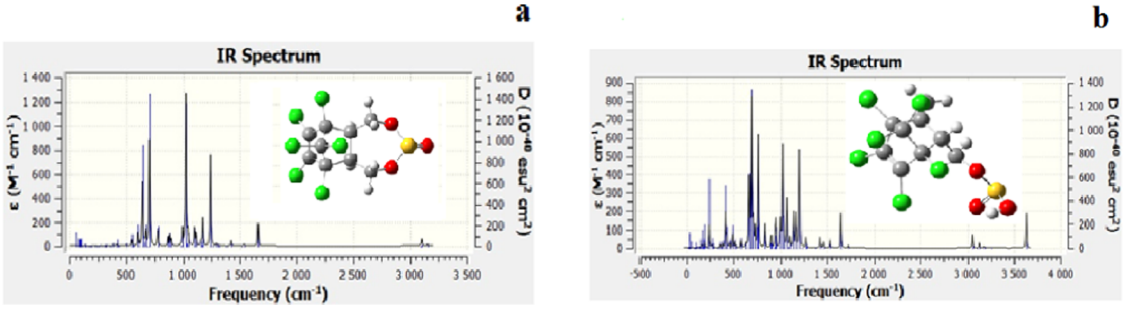

Figure 7. IR spectra for EDS (a) reactant and (b) product calculated at the B3LYP/6-31+G* level; inset: optimized EDS structure.

https://doi.org/10.1021/acsomega.1c03995
ACS Omega 2021, 6, 30515−30525

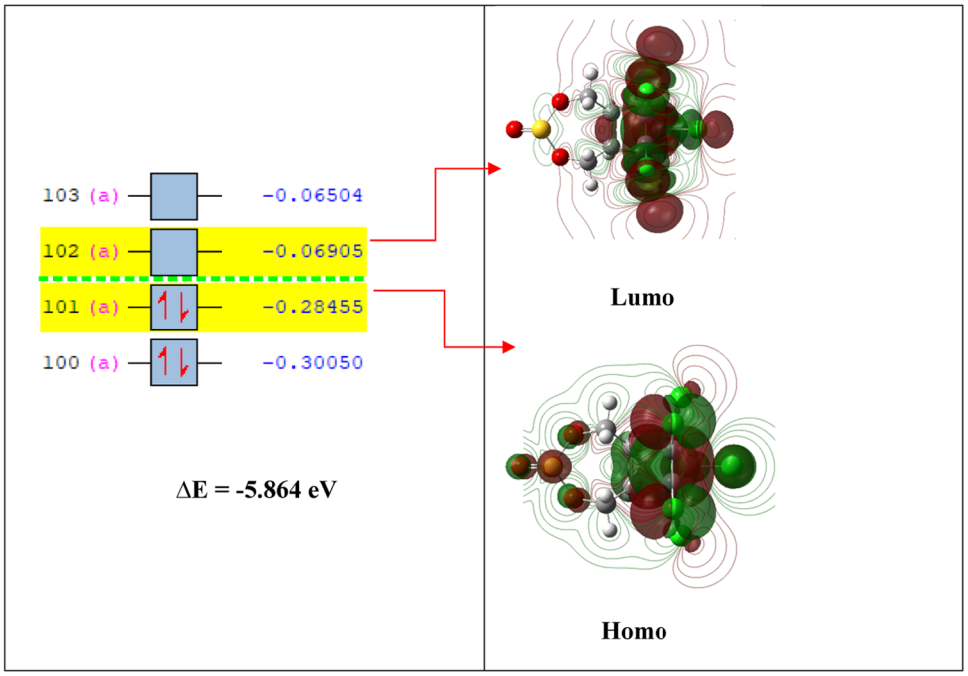

Figure 8. Molecular orbitals of EDS at the B3LYP/6-31+G* level.

Scheme 2. TS Modeling for the Conversion of EDS to Product

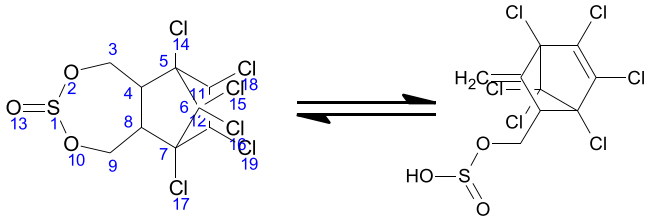

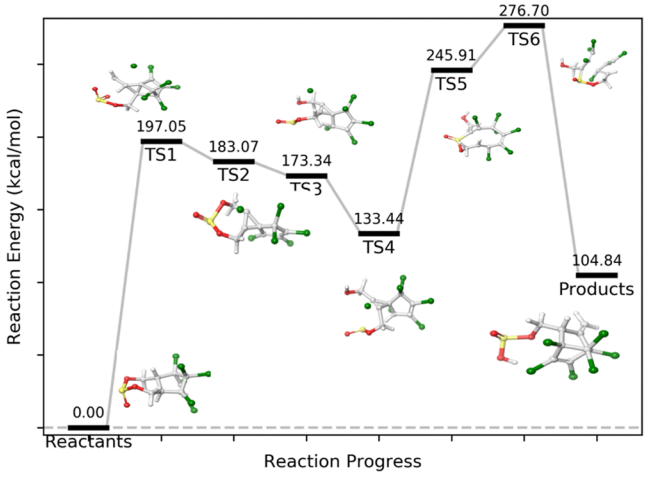

Figure 9. Transition state evolution of the transformation of EDS (isomer 1) to form isomer 96 (1,4,5,6,7,7-hexachloro-3-methylidenebicyclo[2.2.1]hept-5-*en*-2-yl) methyl hydrogen sulfite using Auto TS by Schrödinger molecular modeling suite.

HOMO−LUMO gap of −0.0587 eV is observed, indicating a movement of electron pairs during this transformation. This is also evidenced by a solvation energy of −21.87 kcal mol^{-1}, indicating that this isomer is unstable (Figure 9 and Table 4).

A further decrease in the reaction energy (173.34 kcal mol^{-1}) is observed in the third transition state (TS3) shown in Figure 9. The heterolytic bond of S(2)−(O1) dissociates to form an OH group with C(19). This also includes a double bond between C(6) and (C7) of a cycloprop-2-ene moiety. This isomer exhibits a HOMO−LUMO gap of −0.050 eV and a solvation energy of −20.04 kcal mol^{-1}. It is also worth noting that the solvation energy of TS3 is closer to those of TS1 and TS2, suggesting a similar arrangement of atoms in space.

In Figure 9, the fourth transition state (TS4) includes a slight conformational change of isomer from TS3, with a reaction energy of 133.44 kcal mol^{-1}. This isomer exhibits a HOMO−LUMO gap of −0.0645 eV and a solvation energy of −13.45 kcal mol^{-1}.

In the case of the fifth transition state (TS5), an increase is observed at 245.91 kcal mol^{-1}. This transition is caused by the formation of a σ bond between sulfur and carbon 3. This isomer exhibits a HOMO−LUMO gap of −0.0576 eV and a solvation energy of −13.50 kcal mol^{-1}, indicating an electron transfer reaction (Table 4).

Finally, the sixth transition state (TS6) displays the highest reaction energy of 276.7 kcal mol^{-1}. This is caused by the formation of a π bond between S(2) and C(6). Also, there is a homolytic bond dissociation between C(15)−C(13). This isomer exhibits a HOMO−LUMO gap of −0.1567 eV, indicating an electron transfer, and a solvation energy of −9.86 kcal mol^{-1}, indicating that this isomer has a different arrangement of atoms in space. The product is a stable conformer and revealed a reaction energy of 104.84 kcal mol^{-1} (Table 4). This further confirms that these transformations follow an electron transfer mechanism.

2.2.3. Monte Carlo Adsorption Studies. To further demonstrate the electrocatalytic effect of Fe_3O_4 toward EDS, we measured the adsorption energies for the GCE/f-MWCNT/EDS and GCE/f-MWCNT/Fe_3O_4/EDS systems depicted in Figure 10a1,b2. The total adsorption energies based on the Monte Carlo (MC) simulations demonstrate a

https://doi.org/10.1021/acsomega.1c03995
ACS Omega 2021, 6, 30515−30525

Table 4. Three-Dimensional (3D) Structural Representation of the Starting Structure of EDS, Transition States of Isomers, Product, and Their Associated Energies Obtained by Auto TS

isomer	HOMO	LUMO	ΔE	solvation energy (kcal mol^{-1})	reaction energy (kcal mol^{-1})
reactants	−0.276219	−0.06849	−0.2077	−2.88	0.00
TSI	−0.26409	0.172732	−0.0914	−22.67	197.05
TS2	−0.222435	0.163785	−0.0587	−21.87	183.07
TS3	−0.238635	0.188675	−0.0500	−20.04	173.34
TS4	−0.244979	0.180472	−0.0645	−13.50	123.44
TS5	−0.228762	0.171167	−0.0576	−13.50	245.91
TS6	−0.244596	0.087943	−0.1567	−9.86	276.7
product	0.265334	0.169999	0.095335	−27.40	104.84

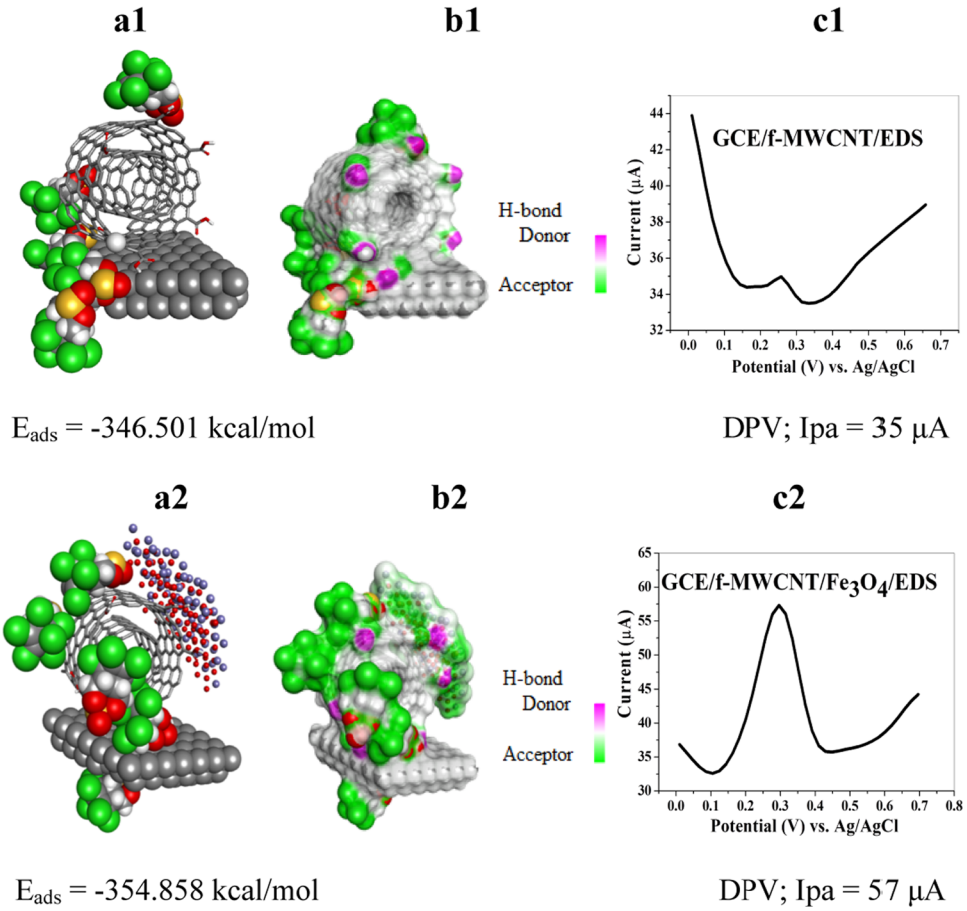

Figure 10. (a−c) Monte Carlo adsorption studies for (a1) GCE/f-MWCNT/EDS and (a2) GCE/f-MWCNT/Fe_3O_4/EDS; H-bond donor−acceptor for (b1) GCE/f-MWCNT/EDS and (b2) GCE/f-MWCNT/Fe_3O_4/EDS; and DPVs of (c1) GCE/f-MWCNT/EDS and (c2) GCE/f-MWCNT/Fe_3O_4/EDS through a layer-by-layer assembly.

greater stabilization of the GCE/f-MWCNT/Fe_3O_4 nanocomposite, attributed to the presence of Fe_3O_4 NPs. It is evident that the latter has a stronger interaction over a wider surface, contributing to a more negative adsorption energy (−354.858 kcal mol^{-1}). This is further demonstrated by the H-bond donor−acceptor representation shown in Figure 10b1,b2. This is a significant result that validates the higher oxidative peak current observed in Figure 10c2 and the amplified CV (Figure 3a).

4. EXPERIMENTAL SECTION

4.1. Materials and Methods. Fe_3O_4 was synthesized from *C. viminalis* leaf extracts. The MWCNTs, EDS, and methanol (HCOH) were procured from Sigma-Aldrich and EMP Millipore Cooperation, Germany, while dimethylformamide $(CH_3)_2NC(O)H$ was purchased from RADCHEM (PTY) Ltd. A 0.1 M phosphate buffer solution (PBS) of pH 7.4 was prepared using sodium phosphate dibasic (NaH_2PO_4; 99%) and monobasic (Na_2HPO_4; 99%), which were obtained from Associated Chemical Enterprise, South Africa. All reagents were of analytical grade, and solutions were prepared with distilled water.

The Metrohm Auto lab potentiostat PGSTAT 302 with 663A Computrace, controlled by NOVA 2.1.4 software, was used for electrochemical experiments in PBS at 25 °C in a three-electrode system consisting of the working, reference, and counter electrodes (WE, RE, CE), respectively. A glassy carbon electrode (GCE) of 3 mm diameter, silver−silver chloride (Ag/AgCl) saturated with 3 M KCl (potassium chloride), and platinum disk were used as WE, RE, and CE,

https://doi.org/10.1021/acsomega.1c03995
ACS Omega 2021, 6, 30515−30525

respectively. A microprocessor pH meter (pH 211 from HANNA instruments) was used for pH measurements.

4.2. Synthesis of Fe_3O_4 and Preparation of MWCNT/Fe_3O_4. The method for the synthesis of Fe_3O_4 and the characterization of the nanocomposite has been adapted from our previously reported studies.[28,37]

4.3. Electrode Modification. The glassy carbon electrode (GCE) was modified by the drop-drying method. Prior to the modification, the GCE was cleaned by gently polishing in an aqueous slurry of alumina nanopowder on a microcloth pad, ultrasonically cleaned in methanol and distilled water, respectively, so as to remove particles of alumina nanopowder and obtain a mirror-like surface, and dried at 40 °C for 3 min. Suspensions of functionalized MWCNT (f-MWCNT), Fe_3O_4, and f-MWCNT/Fe_3O_4 were prepared separately by dispersing 1 mg of f-MWCNT and 3 mg of Fe_3O_4NP in 200 μL of DMF and stirring for 24 h at 60 °C. A 2.5 μL of the formed pastes was dropped on bare GCE and dried in an oven at 40 °C for some time.

4.4. Preparation of the Real Sample. Tomatoes were purchased from an open market and chopped into small pieces, accurately weighed, homogenized, and filtered. One milliliter of the extracted sample juice was diluted with the chosen buffer solution (supporting electrolyte) to 20 mL in an electrochemical cell. The mixture was well mixed, spiked with different concentrations of the analyte stock solution using the standard addition method, and analyzed using differential pulse voltammetry (DPV). The data of DPVs were recorded, and the recovery of the analyte in the sample juice was measured from a calibration plot obtained.

4.5. Voltammetric and Impedimetric Parameters. The parameters for CV were −0.59, 1, −0.60, and −0.59 start, upper vertex, lower vertex, and stop potentials, respectively, and a scan rate of 25 mV s^{-1}. DPV parameters include −0.2, 0.8, and 0.019 V start, stop, and step potentials accordingly. An amplitude of 0.05 V, a scan rate of 30 mV s^{-1}, an interval of 0.5 s, and a conditioning potential of 0.4 V were also used. Parameters for electrochemical impedance spectroscopy (EIS) were the first and last applied frequencies of 100 kHz and 0.1 Hz, respectively, and an applied potential of 0.4 V.

4.6. Computational Methodology. *4.6.1. DFT Calculations.* In this work, the density functional theory (DFT) calculations on the 3D structure of endosulfan geometrically optimized at the B3LYP level using the 6-311+G basis sets were implemented using Gaussian 09.[38] The global minimum for the optimized geometry was further confirmed by a frequency calculation.[39] The energy differences (ΔE) between the highest occupied molecular orbital (HOMO) and the lowest unoccupied molecular orbital (LUMO) are important parameters that define the chemical and electronic properties of any compound, with the smaller value indicating a stronger tendency to donate electrons. For this purpose, the HOMO and LUMO plots for endosulfan were computed at the same level of theory to confirm the oxidative nature of the analyte.

4.6.2. Transition State Search Workflow. Next, the transition state search was performed on Maestro (v12.8).[40] Schrödinger's Graphical User Interface (GUI) was used on an Auto TS panel, which works on a Jaguar module for QM simulations.[36] The two-dimensional (2D) structures of the reactant (EDS) and the proposed product were drawn using the 2D-sketcher tools. Both structures were uploaded into the Auto TS panel and complexes were generated including the reaction paths (i.e., the initial guess for each of the transformations). The full TS experiment was carried out at the B3LYP level of theory and the 6-311+G basis set using water as a solvent.

4.6.3. Monte Carlo Adsorption Studies. To evaluate the interaction of fabricated electrode surfaces, the substrate and adsorbate systems were produced by mimicking the experimental electrodes using a layer-by-layer strategy for the GCE/f-MWCNT/EDS and GCE/f-MWCNT/Fe_3O_4/EDS systems. This was achieved using the Adsorption Locator (AL) module as implemented in the Materials Studio (MS) software.[41] The AL module was used as a preparatory and screening tool with the force field method to obtain a ranking of the energies for each generated configuration, thereby indicating the preferred adsorption sites. The generated adsorbate−substrate conformations for both systems were ranked and the lowest adsorption energy conformers were each optimized using the Forcite−Geometry optimization to reach a stable conformation. The layers of the optimized adsorbate−substrate were used to construct the substrate layers using the "build layer" selection of MS software. Monte Carlo adsorption studies were applied to search the lowest-energy configurations of the adsorbate on the surface of selected substrates as the temperature is gradually decreased.

AUTHOR INFORMATION

Corresponding Author

Krishna Bisetty − *Department of Chemistry, Faculty of Applied Sciences, Durban University of Technology, Durban 4000, South Africa;* orcid.org/0000-0003-4778-2313; Email: bisettyk@dut.ac.za

Authors

Gloria Uwaya − *Department of Chemistry, Faculty of Applied Sciences, Durban University of Technology, Durban 4000, South Africa*

Njabulo Joyfull Gumede − *Department of Chemistry, Mangosuthu University of Technology, Jacobs 4026, South Africa;* orcid.org/0000-0003-4213-5416

Complete contact information is available at: https://pubs.acs.org/10.1021/acsomega.1c03995

Author Contributions

G.U. conceptualized the study, performed electrochemical methodology and investigation, and wrote the original draft. N.J.G. performed the transition state modeling, methodology, and analysis. K.B. supervised, conceptualized, performed DFT and Monte Carlo adsorption studies, methodology, and analysis, and wrote the review and edited it.

Notes

The authors declare no competing financial interest.

ACKNOWLEDGMENTS

We would like to acknowledge the Durban University of Technology for funding and infrastructure support. K.B. acknowledges the Centre for High-Performance Computing (CHPC), Cape Town, South Africa, for all of the computational resources.

REFERENCES

(1) Bakhsh, H.; Buledi, J. A.; Khand, N. H.; Junejo, B.; Solangi, A. R.; Mallah, A.; Sherazi, S. T. H. NiO nanostructures based functional none-enzymatic electrochemical sensor for ultrasensitive determi-

https://doi.org/10.1021/acsomega.1c03995
ACS Omega 2021, 6, 30515−30525

nation of endosulfan in vegetables. *J. Food. Meas. Charact.* **2021**, *15*, 2695−2704.
(2) Bow, Y.; Sutriyono, E.; Nasir, S.; Iskandar, I. Molecularly Imprinted Polymers (MIP) based electrochemical sensors for detection of endosulfan pesticide. *Int. J. Adv. Sci. Engg. Inf. Technol.* **2017**, *7*, No. 662.
(3) Liu, G.; Wang, S.; Liu, J.; Song, D. An electrochemical immunosensor based on chemical assembly of vertically aligned carbon nanotubes on carbon substrates for direct detection of the pesticide endosulfan in environmental water. *Anal. Chem.* **2012**, *84*, 3921−3928.
(4) Quinn, L.; de Vos, J.; Fernandes-Whaley, M.; Roos, C.; Bouwman, H.; Kylin, H.; Pieters, R.; van den Berg, J. Pesticide Use in South Africa: One of the Largest Importers of Pesticides in Africa. In *Pesticides in the Modern World - Pesticides Use and Management*; InTech, 2011; Vol. *1*, pp 49−96.
(5) Mathanakeerthi, S.; Sadheesh, S.; Gowtham, S.; Kumar, V. M. Adsorption of endosulfan from aqueous solution using graphene clay matrix (GCM). *Mater. Today: Proc.* **2021**, *45*, 5665−5671.
(6) Mohammad, A.-M.; Chowdhury, T.; Biswas, B.; Absar, N. Food Poisoning and Intoxication: A Global Leading Concern for Human Health. *Food Safety and Preservation*; Elsevier, 2018; pp 307−352.
(7) James, A.; Emmanuel, D. An overview of endosulfan and the aftermath of its biohazardous administration in Southern India. *Eur. J. Mol. Clin. Med.* **2021**, *8*, 212−218.
(8) Masibi, K. K.; Fayemi, O. E.; Adekunle, A. S.; Al-Mohaimeed, A. M.; Fahim, A. M.; Mamba, B. B.; Ebenso, E. E. Electrochemical Detection of Endosulfan Using an AONP-PANI-SWCNT Modified Glassy Carbon Electrode. *Materials* **2021**, *14*, No. 723.
(9) Jayaraj, R.; Megha, P.; Sreedev, P. Organochlorine pesticides, their toxic effects on living organisms and their fate in the environment. *Interdiscip. Toxicol.* **2016**, *9*, 90−100.
(10) Wilkes, P. S. Gas-liquid chromatographic-mass spectrometric confirmation of endosulfan and endosulfan sulfate in apples and carrots. *J. AOAC Int.* **1981**, *64*, 1208−1210.
(11) Galeano, T.; Guiberteau, A.; Salinas, F. Rapid determination of α-endosulfan and β-endosulfan in formulations and potatoes by high performance liquid chromatography. *Anal. Lett.* **1992**, *25*, 1797−1804.
(12) Castro, J.; Perez, R.; Miguel, E.; Sanchez-Brunete, C.; Tadeo, J. Analysis of endosulfan isomers and endosulfan sulfate in air and tomato leaves by gas chromatography with electron-capture detection and confirmation by gas chromatography−mass spectrometry. *J. Chromatogr. A.* **2002**, *947*, 119−127.
(13) Xu, F.; Liu, L.; Wei, W.; Xu, R. Determination of five endosulfan pesticides in the fish pond water by dispersive liquid−liquid microextraction combined with GC−MS. *Forensic. Sci. Res.* **2017**, *2*, 40−45.
(14) Watson, K.; Lepore, J. Radiative corrections to nuclear forces in the pseudoscalar meson theory. *Phys. Rev.* **1949**, *76*, 1157−1163.
(15) Rathnakumar, S. S.; Noluthando, K.; Kulandaiswamy, A. J.; Rayappan, J. B. B.; Kasinathan, K.; Kennedy, J.; Maaza, M. Stalling behaviour of chloride ions: a non-enzymatic electrochemical detection of α-Endosulfan using CuO interface. *Sens. Actuators, B* **2019**, *293*, 100−106.
(16) El Bakouri, H.; Palacios-Santander, J. M.; Cubillana-Aguilera, L.; Ouassini, A.; Naranjo-Rodríguez, I.; de Cisneros, J. L. H.-H. Electrochemical analysis of endosulfan using a C18-modified carbon-paste electrode. *Chemosphere* **2005**, *60*, 1565−1571.
(17) Solanki, P.; Kaushik, A.; Agrawal, V.; Malhotra, B. Nano-structured metal oxide−based sensors. *NPG Asia Mater.* **2011**, *3*, 17−24.
(18) Khan, I.; Saeed, K.; Khan, I. Nanoparticles: Properties, applications and toxicities, Arab. *Arabian J. Chem.* **2019**, *12*, 908−931.
(19) Kumaravel, A.; Chandrasekaran, M. A novel nanosilver/nafion composite electrode for electrochemical sensing of methyl parathion and parathion. *J. Electroanal. Chem.* **2010**, *638*, 231−235.
(20) Power, A. C.; Morrin, A. Electroanalytical Sensor Technology. In *Electrochemistry*; Intech, 2013; pp 141−178.
(21) Magar, H. S.; Ghica, M. E.; Abbas, M. N.; Brett, C. M. A. A novel sensitive amperometric choline biosensor based on multiwalled carbon nanotubes and gold nanoparticles. *Talanta* **2017**, *167*, 462−469.
(22) Sajjadi, S.; Ghourchian, H.; Rafiee-Pour, H.-A.; Rahimi, P. Accelerating the electron transfer of choline oxidase using ionic-liquid/NH 2-MWCNTs nano-composite. *J. Iran. Chem. Soc.* **2012**, *9*, 111−119.
(23) Ahmed, D. S.; Haider, A. J.; Mohammad, M. Comparesion of functionalization of multi-walled carbon nanotubes treated by oil olive and nitric acid and their characterization. *Energy Procedia* **2013**, *36*, 1111−1118.
(24) Rajarao, R.; Jayanna, R.; Sahajwalla, V.; Bhat, B. R. GreenApproach to decorate multi-walled carbon nanotubes by metal/metal oxide nanoparticles. *Procedia Mater. Sci.* **2014**, *5*, 69−75.
(25) Saleh, T. A.; Siddiqui, M. N.; Al-Arfaj, A. A. Synthesis of multiwalled carbon nanotubes-titania nanomaterial for desulfurization of model fuel. *J. Nanomater.* **2014**, *2014*, 1−6.
(26) Goswami, B.; Mahanta, D. Fe3O4-Polyaniline Nanocomposite for Non-enzymatic Electrochemical Detection of 2,4-Dichlorophenoxyacetic Acid. *ACS Omega* **2021**, *6*, 17239−17246.
(27) Qu, J.; Dong, Y.; Wang, Y.; Xing, H. A novel sensor based on Fe3O4 nanoparticles−multiwalled carbon nanotubes composite film for determination of nitrite. *Sens. Bio-Sens. Res.* **2015**, *3*, 74−78.
(28) Uwaya, G. E.; Fayemi, O. E. Electrochemical detection of choline at f-MWCNT/Fe3O4 nanocomposite modified glassy carbon electrode. *Mater. Res. Express.* **2021**, *8*, No. 055403.
(29) Fayemi, O. E.; Adekunle, A. S.; Ebenso, E. E. Electrochemical determination of serotonin in urine samples based on metal oxide nanoparticles/MWCNT on modified glassy carbon electrode. *Sens. Bio-Sens. Res.* **2017**, *13*, 17−27.
(30) Xu, Z.; Fan, X.; Ma, Q.; Tang, B.; Lu, Z.; Zhang, J.; Ye, J.; et al. A sensitive electrochemical sensor for simultaneous voltammetric sensing of cadmium and lead based on Fe3O4/multiwalled carbon nanotube/laser scribed graphene composites functionalized with chitosan modified electrode. *Mater. Chem. Phys.* **2019**, *238*, No. 121877.
(31) Ghapanvari, M.; Madrakian, T.; Afkhami, A.; Ghoorchian, A. A modified carbon paste electrode based on Fe 3 O 4@ multi-walled carbon nanotubes@ polyacrylonitrile nanofibers for determination of imatinib anticancer drug. *J. Appl. Electrochem.* **2020**, *50*, 281−294.
(32) Filik, H.; Avan, A. A.; Aydar, S. Square-wave adsorptive stripping voltammetric determination of serotonin at glassy carbon electrode modified with Safranine O. *Int. J. Electrochem. Sci.* **2014**, *9*, 2922−2933.
(33) Fayemi, O. E.; Adekunle, A. S.; Ebenso, E. E. Metal oxide nanoparticles/multi-walled carbon nanotube nanocomposite modified electrode for the detection of dopamine: comparative electrochemical study. *J. Biosens. Bioelectron.* **2015**, *6*, No. 1000190.
(34) Wang, J. *Analytical Electrochemistry*, 2nd ed., Wiley-VCH, New York, 2000, pp 1−205.
(35) Gowda, J. I.; Nandibewoor, S. T. Electrochemical behavior of paclitaxel and its determination at glassy carbon electrode. *Asian J. Pharm. Sci.* **2014**, *9*, 42−49.
(36) Schrödinger Release 2021-2: Jaguar, Schrödinger, LLC, New York, 2021.
(37) Uwaya, G. E.; Fayemi, O. E.; Sherif, E. S. M.; Junaedi, H.; Ebenso, E. E. Synthesis, electrochemical studies, and antimicrobial properties of Fe3O4 nanoparticles from Callistemon viminalis plant extracts. *Mater* **2020**, *13*, No. 4894.
(38) Frisch, G. W. T. M. J.; Schlegel, H. B.; Schlegel, G. E.; Robb, M. A.; Cheeseman, J. R.; Scalmani, G.; Barone, V.; Petersson, G. A.; Nakatsuji, H.; Li, X.; Caricato, M.; Marenich, A. V.; Bloino, J.; Janesko, B. G.; Gomperts, R.; Mennucci, B.; Hratchian, H. P.; Ortiz, J. V.; Izmaylov, A. F.; Sonnenberg, J. L.; Williams, D. Y.; Ding, F.; Lipparini, F.; Egidi, F.; Goings, J.; Peng, B.; Petrone, A.; Henderson, T.; Ranasinghe, D.; Zakrzewski, V. G.; Gao, J.; Rega, N.; Zheng, G.; Liang, W.; Hada, M.; Ehara, M.; Toyota, K.; Fukuda, R.; Hasegawa, J.; Ishida, M.; Nakajima, T.; Honda, Y.; Kitao, O.; Nakai, H.; Vreven, T.;

https://doi.org/10.1021/acsomega.1c03995
ACS Omega 2021, 6, 30515−30525

Throssell, K.; Montgomery, J. A.; Peralta, J. E., Jr.; Ogliaro, F.; Bearpark, M. J.; Heyd, J. J.; Brothers, E. N.; Kudin, K. N.; Staroverov, V. N.; Keith, T. A.; Kobayashi, R.; Normand, J.; Raghavachari, K.; Rendell, A. P.; Burant, J. C.; Iyengar, S. S.; Tomasi, J.; Cossi, M.; Millam, J. M.; Klene, M.; Adamo, C.; Cammi, R.; Ochterski, J. W.; Martin, R. L.; Morokuma, K.; Farkas, O.; Foresman, J. B.; Fox, D. J. *Gaussian 09*, revision A.02, Gaussian, Inc., Wallingford CT,2016.

(39) Sheikhi, M.; Shahab, S.; Khaleghian, M.; Kumar, R. Interaction between new anti-cancer drug syndros and CNT (6, 6-6) nanotube for medical applications: geometry optimization, molecular structure, spectroscopic (NMR, UV/Vis, excited state), FMO, MEP and HOMO-LUMO investigation. *Appl. Surf. Sci.* **2018**, *434*, 504−513.

(40) Maestro, Schrödinger, LLC, New York, 2021.

(41) Biovia, D. S.. *Material Studio Modelling*, v. 16.1. 0, Dassault Systemes, San Diego, 2016.

https://doi.org/10.1021/acsomega.1c03995
ACS Omega 2021, 6, 30515−30525